ACSNANO

www.acsnano.org

ARTICLE

Highly Efficient Electric-Field Control of Giant Rashba Spin–Orbit Coupling in Lattice-Matched InSb/CdTe Heterostructures

Yong Zhang,[▽] Fenghua Xue,[▽] Chenjia Tang, Jiaming Li, Liyang Liao, Lun Li, Xiaoyang Liu, Yumeng Yang, Cheng Song, and Xufeng Kou*

Cite This: ACS Nano 2020, 14, 17396–17404 Read Online

ACCESS | Metrics & More | Article Recommendations | Supporting Information

ABSTRACT: **Spin–orbit coupling (SOC), the relativistic effect describing the interaction between the orbital and spin degrees of freedom, provides an effective way to tailor the spin/magnetic orders using electrical means. Here, we report the manipulation of the spin–orbit interaction in the lattice-matched InSb/CdTe heterostructures. Owing to the energy band bending at the heterointerface, the strong Rashba effect is introduced to drive the spin precession where pronounced weak antilocalization cusps are observed up to 100 K. With effective quantum confinement and suppressed bulk conduction, the SOC strength is found to be enhanced by 75% in the ultrathin InSb/CdTe film. Most importantly, we realize the electric-field control of the interfacial Rashba effect using a field-effect transistor structure and demonstrate the gate-tuning capability which is 1–2 orders of magnitude higher than other materials. The adoption of the InSb/CdTe integration strategy may set up a general framework for the design of strongly spin–orbit coupled systems that are essential for CMOS-compatible low-power spintronics.**

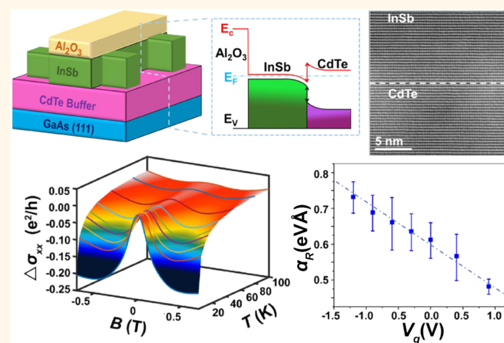

KEYWORDS: *spin–orbit coupling, Rashba effect, weak antilocalization effect, electric-field control, heterostructure engineering*

When electrons move in a solid, their spin states are subjected to the spin–orbit coupling (SOC) term that is described by the relativistic Dirac Hamiltonian:[1]

$$H_{so} = -\frac{e\hbar}{(2m^{*}c)^{2}}\boldsymbol{\sigma}\cdot\boldsymbol{B}_{\text{eff}} = -\frac{e\hbar}{(2m^{*}c)^{2}}\boldsymbol{\sigma}\cdot(\boldsymbol{p}\times\boldsymbol{E}) \quad (1)$$

where e is the electron charge, $\hbar$ is the reduced Planck constant, m^* is the electron effective mass, c is the speed of light, $\boldsymbol{\sigma}$ is the Pauli spin matrix vector, and $\boldsymbol{B}_{\text{eff}}$ is the magnetic effective field determined by the product of the momentum operator $\boldsymbol{p}$ and the electric field $\boldsymbol{E}$. Accordingly, strong SOC can be generated in materials with a large atomic potential gradient (*i.e.*, $\boldsymbol{E} = \nabla V$), and a multitude of heavy metals and narrow-band semiconductors have been utilized to explore emerging spin–orbit effects.[2–6] Moreover, when the SOC is strong enough to invert the conduction and valence bands, the resulting topological insulators/semimetals with spin-polarized states have unleashed progressive development of spintronics and topological quantum physics in the past decade.[7–13] Alternatively, following the guidance of eq 1, a large built-in electric field introduced at the inversion–asymmetric hetero-interface can also lift the spin degeneracy (*i.e.*, Rashba effect).[14–16] Compared with the bulk materials, heterostructures take full advantage of band engineering and interfacial/low-dimensional effects, hence enabling the spin accumulation and precession in an electrically controllable manner, which is of particular importance for magnetic-based nonvolatile logic and memory computation.[17–19]

In order to further enrich the candidate pool that is more suitable to regulate spin/magnetic orders, opportunities may lie in the incorporation of large SOC materials into the heterostructure/superlattice forms through appropriate structural optimization, and recent efforts have been applied to design heavy metal/topological quantum material-based hybrid systems with nontrivial interface/surface states.[20–22] In this article, we make use of the lattice-matched InSb/CdTe

Received: September 9, 2020
Accepted: December 4, 2020
Published: December 10, 2020

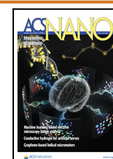

Downloaded via SHANGHAITECH UNIV on June 1, 2023 at 06:36:14 (UTC). See https://pubs.acs.org/sharingguidelines for options on how to legitimately share published articles.

© 2020 American Chemical Society

https://dx.doi.org/10.1021/acsnano.0c07598
ACS Nano 2020, 14, 17396–17404

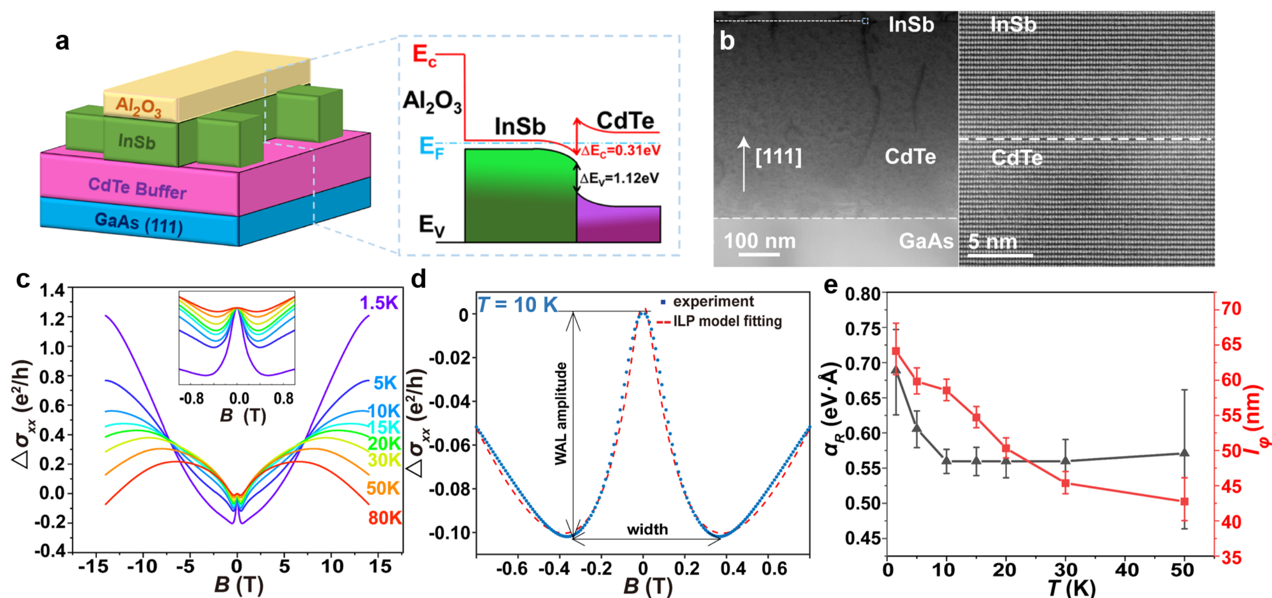

Figure 1. Weak antilocalization effect in the InSb(15 nm)/CdTe(1.2 μm) heterostructures. (a) Schematic of the Al_2O_3/InSb/CdTe structure on the GaAs substrate and relevant energy band diagram. The strong band bending and large conduction band offset at the InSb/CdTe interface warrant the well-defined 2D conduction channel with large interfacial Rashba SOC strength. (b) HRSTEM image highlights the highly ordered crystalline configuration across the InSb/CdTe interface with negligible defects. (c) Temperature-dependent magnetoconductance results. As temperature decreases, the MC curves show the negative-to-positive transition. Inset: Pronounced WAL cusps are observed from 1.5 to 80 K. (d) Fitting the WAL data with the ILP model. The amplitude and width of the WAL cusp characterize the phase-coherent transport and Rashba SOC, respectively. (e) Temperature-dependent Rashba coefficient and phase-coherent length.

heterostructures as the platform to showcase the highly tunable interfacial Rashba effect by a top-gate voltage. For the narrow-band semiconductor InSb, it is known that the small band gap (E_g = 0.18 eV) ensures the strong intrinsic SOC, and the ultrahigh electron mobility (μ > 40,000 $cm^2 \cdot V^{-1} \cdot s^{-1}$ in thick InSb films and sandwich quantum wells at 300 K) may enable long phase-coherent/scattering length and high-speed operation at room temperature.[23] More importantly, when the InSb layer is adjacent to the wide-gap semiconductor CdTe with the same lattice constant, the type-I quantum well with a large conduction band offset (ΔE_C = 0.31 eV) will be formed at the atomically flat heterointerface (Figure 1a).[24] As a result, the strong band bending in the integrated InSb/CdTe heterostructures would not only confine the coherent electron conduction in the defect-free channel (*i.e.*, two-dimensional electron gas, 2DEG) but also serve as the fountainhead of the interfacial Rashba interaction that can be manipulated electrically.[25] With further dedicated interfacial element-bonding and critical thickness selection, it is predicted that the large internal polar field at the InSb/CdTe interface may trigger the band inversion and give rise to a topologically nontrivial edge state with a giant Rashba-type spin splitting.[26] Consequently, all these salient features hosted in the InSb/CdTe system, if they can be experimentally implemented, could offer more flexibilities in controlling versatile spin−orbit dynamics for low-power spintronic applications.

RESULTS AND DISCUSSION

Large WAL Effect and Rashba Coefficient in InSb/CdTe Heterostructures. To elucidate the aforementioned proposal, high-quality lattice-matched InSb/CdTe heterostructures are grown on the 3 in. semi-insulating GaAs(111)B substrate *via* molecular beam epitaxy (MBE).[27] The use of the (111) crystal orientation can facilitate the fast strain relaxation and limit the dislocation formation during the initial CdTe nucleation stage. Subsequently, the obtained smooth CdTe buffer layer helps to promote the layer-by-layer growth of the single-crystalline InSb thin film, and the sharp InSb/CdTe heterointerface with well-ordered zinc-blende configuration and negligible crystallographic defects is confirmed by the high-resolution scanning transmission electron microscopy (HRSTEM) in Figure 1b.

After sample preparation, we carry out standard four-point magneto-transport measurements on the InSb(15 nm)/CdTe-(1.2 μm) Hall bar device with a dimension of 1.5 mm × 3 mm. Figure 1c displays the temperature-dependent normalized longitudinal magnetoconductance (MC) $\Delta\sigma_{xx} = \sigma_{xx}(B) - \sigma_{xx}(0)$ results as a function of the external magnetic field. In opposite to the Lorentz force-driven negative MC background (*i.e.*, $\sigma_{xx} \propto 1/(1 + \mu B^2)$) of bulk InSb, the thin InSb/CdTe sample exhibits an obvious negative-to-positive MC evolution trend as the temperature drops from 80 K, and its overall contour is dominated by a marked positive MC exceeding 100% in 14 T at 1.5 K (*i.e.*, corresponding to a negative magnetoresistance in Figure S1a). It is noted that similar positive MC behaviors under large perpendicular magnetic fields have also been observed in the $LaAlO_3/SrTiO_3$ heterostructures, and its origin may relate to the presence of the strong spin−orbit interaction that affects the electron transport in the 2DEG channel at the interface.[28]

In addition to the positive MC curve, the quantum interference-induced conductance correction, namely the weak-antilocalization (WAL) effect, represents another intriguing feature of the MBE-grown InSb/CdTe heterostructures. Given that the coherent electron propagation is intrinsically related to the spin and electronic band structure (*i.e.*, Berry phase) at the Fermi level, WAL is served as the hallmark to evaluate the SOC in solid-state systems.[29] As highlighted in the

https://dx.doi.org/10.1021/acsnano.0c07598
ACS Nano 2020, 14, 17396−17404

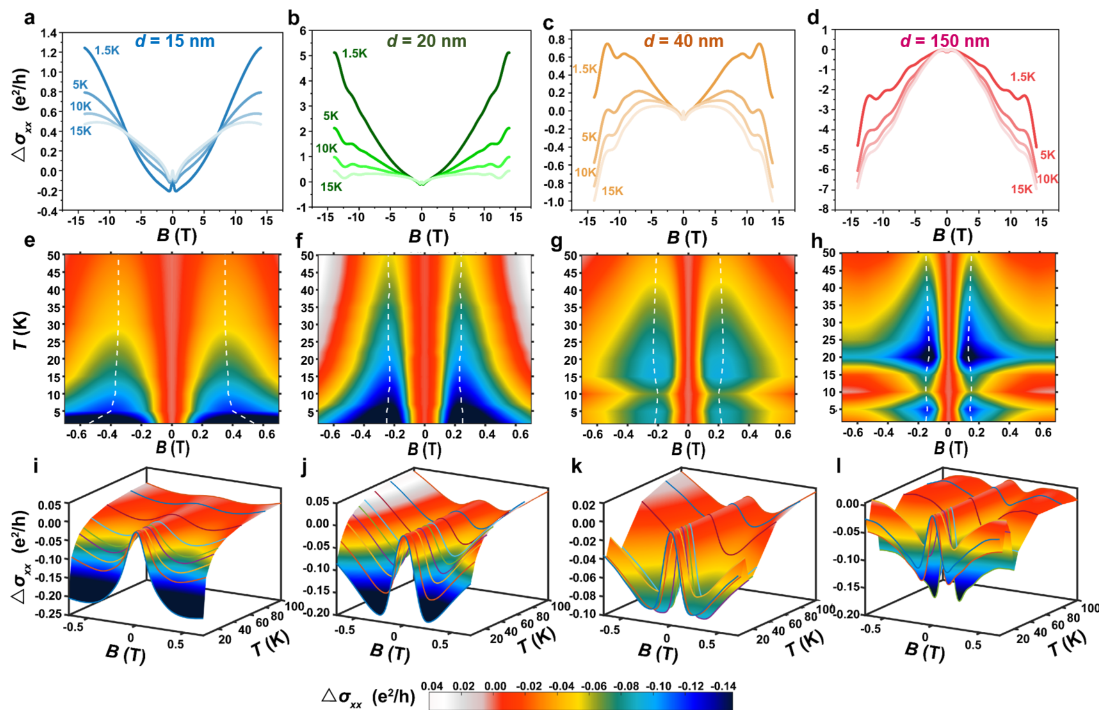

Figure 2. Thickness-dependent WAL phase diagram of the InSb/CdTe heterostructures. All the four samples have the same growth condition and CdTe buffer layer (1.2 μm) configuration but different InSb layer thicknesses of d = 15, 20, 40, and 150 nm, respectively. (a−d) Temperature-dependent large-field MC results. With the increase of the top InSb layer, the overall transport behavior is dominated by the InSb bulk conduction with negative MC background and SdH quantum oscillations. Temperature-dependent WAL data of the four samples plot within the (e−h) [1.5 K, 50 K] and (i−l) [1.5 K, 100 K] regimes. Same color code is used for a direct comparison, and the white dash-lines in (e−h) indicate the WAL width of each sample.

inset of Figure 1c, the sharp positive MC cusp is well-developed in the low magnetic-field regime and maintains its characteristic line shape up to 80 K. Compared with other reported material candidates,[14,30−37] the WAL phenomena observed in the InSb/CdTe sample is most significant in terms of both the large amplitude ($\Delta\sigma_{xx}$ = 0.2 e^2/h) and wide width (magnetic-field range = ± 0.54 T at 1.5 K), as defined in Figure 1d. In order to quantitatively investigate the large WAL in the mm-size InSb(15 nm)/CdTe(1.2 μm) device, we apply the Iordanskii, Lyanda-Geller, and Pikus (ILP) model whose explicit expression is described as[38]

$$\Delta\sigma_{xx}(\boldsymbol{B}) = \frac{-e^2}{4\pi^2\hbar}\left[\begin{array}{l} 3C + \dfrac{1}{a_0} + \dfrac{2a_0 + 1 + \frac{B_{so}}{B}}{a_1\left(a_0 + \frac{B_{so}}{B}\right) - 2\frac{B_{so}}{B}} \\ -\Bigg(\displaystyle\sum_{n=1}^{\infty} \frac{3}{n} \\ \quad - \dfrac{2a_n{}^2 + 2\frac{B_{so}}{B}a_n - 1 - 2(2n+1)\frac{B_{so}}{B}}{\left(a_n + \frac{B_{so}}{B}\right)a_{n-1}a_{n+1} - 2\frac{B_{so}}{B}[(2n+1)a_n - 1]}\Bigg) \\ + 2\ln\left(\dfrac{\boldsymbol{B}_{tr}}{\boldsymbol{B}}\right) + \Psi\left(\dfrac{1}{2} + \dfrac{\boldsymbol{B}_{\varphi}}{\boldsymbol{B}}\right) \end{array}\right] \quad (2)$$

where C is the Euler's constant, Ψ is the digamma function, $\boldsymbol{B}_{so}$, $\boldsymbol{B}_{\varphi}$, $\boldsymbol{B}_{tr}$ are the characteristic effective magnetic fields gauging the first-order interfacial Rashba interaction, phase-coherent transport, and momentum scattering process in the system, respectively, and the coefficient $a_n = n + \frac{1}{2} + \frac{B_{\varphi}}{B} + \frac{B_{so}}{B}$. Since the carrier mobility (μ = 650−1000 cm^2·V^{-1}·s^{-1} from 1.5 to 80 K) can be obtained from the Hall measurement, $\boldsymbol{B}_{tr} = \hbar/4D\mu m^*$ (D is the diffusion constant) is determined, therefore leaving $\boldsymbol{B}_{so}$ and $\boldsymbol{B}_{\varphi}$ the only two fitting parameters. As identified in Figure 1d, the wide WAL width highlights the strong SOC strength, and the amplitude of the WAL effect is closely linked with the ratio of the phase-breaking and spin-relaxation rates in the InSb/CdTe system. By further converting the fitted $\boldsymbol{B}_{so}$ and $\boldsymbol{B}_{\varphi}$ into Rashba coefficient $\alpha_R = \sqrt{e^3\hbar\boldsymbol{B}_{so}}/m^*$ and phase-coherent length $l_{\varphi} = \sqrt{\hbar/4e\boldsymbol{B}_{\varphi}}$, we plot their temperature-dependent results in Figure 1e (detail information is elaborated in Supporting Information S2). As the sample is cooled down, the magnitude of α_R first stabilizes at 0.56 eV·Å in the high-temperature region and then experiences a dramatic increase up to 0.7 eV·Å when T < 10 K. Compared with the classical InSb/InAlSb quantum well structure (α_R = 0.05−0.14 eV·Å),[23,31,39] the large enhancement of α_R in our InSb/CdTe sample may stem from the better band confinement due to the larger ΔE_C and improved heterointerface quality. In the meantime, the phase-coherent length l_{φ} decreases monotonically with elevated temperature, and the power-law correlation may suggest the electron−electron scattering mechanism in our device (Supporting Information S3).[40] Nevertheless, we need to point out that the extracted l_{φ} is always longer than the spin−orbit relaxation length (l_{so} ~ 25 nm) for 1.5 K < T < 80 K, thus guaranteeing the observation of the quantum interference signals in the whole temperature regime. Besides, the inversely proportional relationship between spin−orbit relaxation time ($\tau_{so} = \hbar/4eD\boldsymbol{B}_{so}$) and the momentum scattering time ($\tau_{tr} = \mu m^*/e$) justifies that the spin-relaxation process is indeed associated with the spin-precession in which the effective magnetic field $\boldsymbol{B}_{eff}$ is originated from the interfacial Rashba

https://dx.doi.org/10.1021/acsnano.0c07598
ACS Nano 2020, 14, 17396−17404

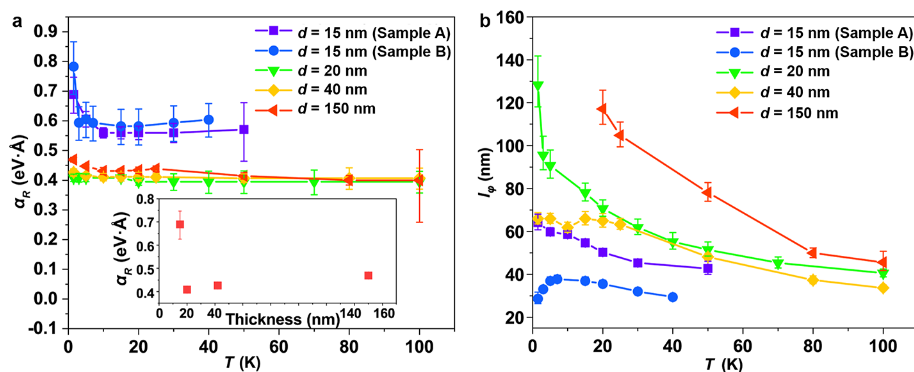

Figure 3. Thickness-dependent Rashba coefficient and phase-coherent length of the InSb/CdTe thin films. (a) Temperature-insensitive α_R slopes of the d = 20, 40, 150 nm samples coincide with each other, manifesting the fully developed 2D conduction channel with the same Rashba SOC origin in thick samples. On the other hand, the two d = 15 nm samples, with similar carrier density but different carrier mobilities, exhibit almost the same $\alpha_R - T$ scaling behavior. Inset: Thickness-dependent α_R enlarges from 0.4 eV·Å to 0.7 eV·Å when d < 20 nm. (b) The phase-coherent length shows a positive correlation with the InSb layer thickness and decreases monotonically with elevated temperature.

interaction (*i.e.*, D'yakonov–Perel mechanism), and it also validates the analysis of the magneto-transport data with the ILP model throughout this work (see Supporting Information S4).[41] To conclude, the pronounced WAL effect and large Rashba coefficient possessed in the lattice-matched InSb/CdTe heterostructures warrant a promising potential for energy-efficient spintronic applications.

Mapping the Thickness-Dependent WAL Phase Diagram. Inspired by the discoveries in Figure 1, we further prepare a set of InSb/CdTe(1.2 μm) thin films by varying the top InSb layer thickness d, for which Figure 2 lists the systematic results on four selected samples with d = 15, 20, 40, and 150 nm. By comparing their magneto-transport data in Figure 2a–d, it can be clearly seen that the overall MC slope undergoes a positive-to-negative transition with the increase of the InSb layer thickness, and the pronounced high-field Shubnikov de Haas (SdH) quantum oscillations in thick samples signify the high-mobility (*i.e.*, increase with InSb layer thickness) and large g-factor of the InSb layer. However, unlike the InSb bulk conduction, universal WAL effects are observed in all samples across the whole examined temperature range (*i.e.*, we have confirmed the 2D nature of the WAL cusps as the $\sigma_{xx} - \log(T)$ slopes of these four Hall-bar devices all follow a linear relation, as discussed in Figure S5).[42] To better visualize such Rashba effect-induced WAL phenomena, we summarize the low-field MC information on each sample with respect to temperature and applied magnetic field and present the three-dimensional (3D) plots in Figure 2e–l (*i.e.*, we have chosen the same color code in all figures for a fair comparison). The corresponding WAL phase diagrams reveal two unusual features. First, the WAL width remains almost constant around ±0.2 T in all $d \geq 20$ nm samples, whereas it enlarges to ±0.4 T and discloses a clear temperature-dependent trait below 10 K for the InSb(15 nm)/CdTe(1.2 μm) case. Second, instead of the gradual attenuation of the WAL amplitudes in Figure 2e,f, the $\Delta\sigma_{xx}$ peak values of the d = 40 and 150 nm samples do not appear at the lowest temperature T = 1.5 K, which may imply the multichannel conduction scenario in thick InSb/CdTe heterostructures.

In light of the importance of the thickness-dependent WAL phase diagram and its underlying physical origin, the same ILP model fitting procedure is applied on the four InSb/CdTe samples, and the calculated α_R and l_φ datasheets are provided in Figure 3. Consistent with the traces of the white dashed-lines depicted in Figure 2e–h, the temperature-dependent Rashba coefficient can be divided into two distinct categories regarding the InSb layer thickness. Specifically, the relatively constant α_R = 0.4 eV·Å may indicate the intrinsic temperature-invariant property of the 2D conduction along the fully developed quantum well in thick InSb/CdTe heterostructures. By contrast, the dimension reduction along the z-axis could modify the band bending situation at the InSb/CdTe interface, thus giving rise to the enhancement of α_R by more than 75% in the thinnest sample at T = 1.5 K, as captured in the inset of Figure 3a. Meanwhile, the sheet carrier density (n_{2D}) in the InSb(15 nm)/CdTe(1.2 μm) film is also found to be more sensitive to the temperature variation, namely the carrier freeze-out effect helps to suppress n_{2D} at deep cryogenic temperatures (Supporting Information S6). Given the positive correlation between the carrier density and the electron effective mass of InSb,[43] the lighter electrons act as another boosting factor for the sharp increase of the Rashba coefficient $\alpha_R = \sqrt{e^3\hbar \boldsymbol{B}_{so}}/m^*$ when T < 10 K. Moreover, although in general l_φ is longer in thicker InSb layer (Figure 3b), yet we need to emphasize that the phase-coherent scattering process has little impact on the thickness-dependent α_R scaling behavior. To address this point, we have grown another InSb(15 nm)/CdTe(1.2 μm) sample (sample B) with a similar carrier density (n_{2D} = 6–7 × 10^{11} cm^{-2}) but much lower phase-coherent length (l_φ = 40 nm). As illustrated in Figure 3a, the temperature-dependent α_R curves of both d = 15 nm thin films are similar to each other (*i.e.*, the 3D MC plots of sample B also resemble those of sample A, as shown in Figure S7). Based on these findings, it is suggested that structural engineering *via* quantum confinement may play an indispensable role in tailoring the interfacial Rashba SOC strength of our InSb/CdTe heterostructures.

Electric-Field Control of Rashba Interaction in the Top-Gated InSb/CdTe Device. As we addressed in the introduction, the unparalleled advantage for heterostructures-based spintronics lies in the electric-field control capability. Accordingly, we further deposit a 50 nm Al_2O_3 thin film on top of the 3 in. InSb(15 nm)/CdTe(1.2 μm) wafer as the high-κ dielectric layer and design the top-gated field-effect transistor (FET) using a multistep photolithography and ion-beam

https://dx.doi.org/10.1021/acsnano.0c07598
ACS Nano 2020, 14, 17396–17404

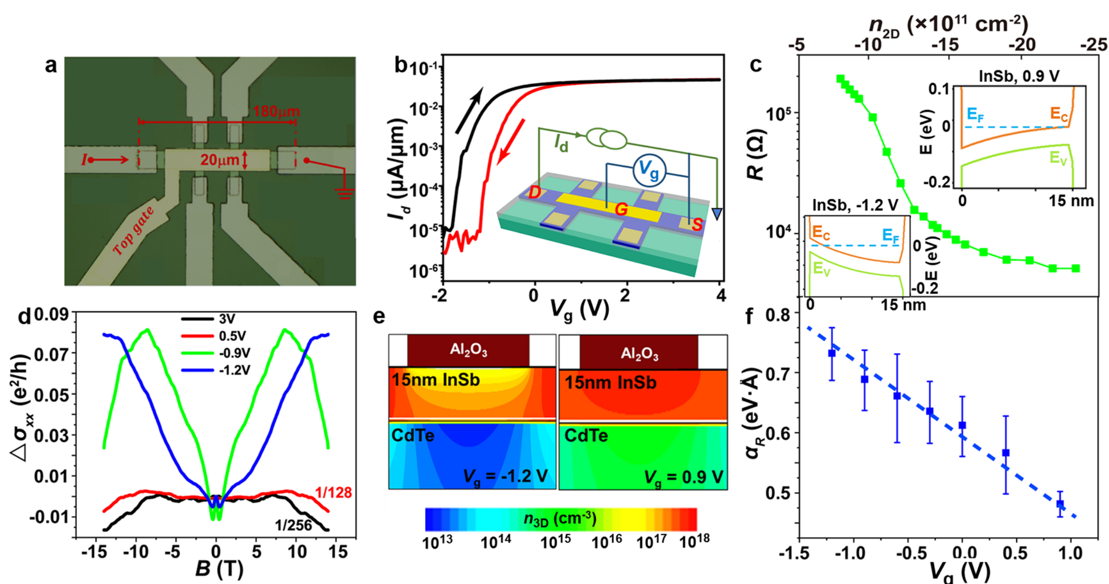

Figure 4. Electric field control of the interfacial Rashba SOC strength in the top-gated InSb(15 nm)/CdTe(1.2 μm) FET device. (a) Optical microscopy image of the fabricated device with the gate size of 100 μm (length) × 20 μm (width). (b) I_d−V_g transfer characteristics of the FET at 1.5 K. Both the large ON/OFF ratio and narrow hysteresis gate-sweeping window underline the high device performance. Inset: Illustration of the top-gated FET device structure with I−V measurement setup. (c) Gate-dependent channel resistance and carrier density at T = 1.5 K. Inset: Real-space band diagrams of the device under V_g = −1.2 V (lower left panel) and 0.9 V (upper right panel), respectively. (d) Gate-controlled MC curves of the FET device. When the carrier density of the InSb channel is tuned to n_{2D} = 7 × 10^{-11} cm^{-2} at V_g = −1.2 V, the MC line-shape is similar to the purple line of Figure 1c, while the WAL signal is almost suppressed in the heavily n-type region. (e) TCAD-simulated carrier density distribution profile in the FET structure at V_g = −1.2 V (left panel) and 0.9 V (right panel). Along with the band bending situation, it is seen that the main electron conduction channel switches from the InSb/CdTe interface to the Al_2O_3/InSb side when the applied gate voltage varies from −1.2 V to +0.9 V. (f) The Rashba coefficient displays a nearly linear relationship with the applied top-gate voltage. When V_g > 0.9 V, the WAL signal becomes too weak, and α_R cannot be extracted any more.

etching process. Figure 4a shows an optical microscope image of the fabricated device structure with a gate aspect ratio of 100 μm (length) × 20 μm (width). After device fabrication, electric-field controlled measurements are carried out at low temperatures. As shown in Figure 4b,c, the near linear relationship between the electron density and the gate voltage, along with the narrow hysteresis gate-sweeping window, not only reflects high Al_2O_3/InSb interface quality but also allows for efficient gate manipulation. Consequently, by successively applying the top gate voltage V_g between ±2 V, the I−V transfer characteristics unveil a large ON/OFF ratio of 10^4 (Figure 4b), and the InSb channel resistance can also be changed by 100 times (Figure 4c), both of which are at least 2 orders of magnitude larger than the topological quantum materials and heavy metal counterparts.[44,45] Concurrently, the magnetoconductance of the FET device also displays a striking response to the applied gate voltage at T = 1.5 K. In particular, the combination of the low-field WAL cusp and high-field positive background governs the MC curve in the V_g < 0 V regime. When the carrier density (n_{2D} = 7 × 10^{11} cm^{-2} at V_g = −1.2 V) is tuned to the same level as the pristine InSb(15 nm)/CdTe(1.2 μm) sample, the WAL width and MC line-shape (blue line in Figure 4d) coincide with mm-size Hall-bar data (purple line in Figure 1c), again manifesting the scale-invariant nature of the interfacial Rashba effect with identical structure and carrier density (*i.e.*, yet the magnitude of the WAL cusp is more vulnerable to device fabrication process which may deteriorate the phase coherent length in the μm-size device). On the contrary, once the positive bias is applied on the device, the low-field MC is overwhelmed by a rather flat background, and the weak WAL signal becomes indistinguishable when V_g > 0.9 V. Furthermore, from the summarized α_R−V_g slope in Figure 4f, it is verified that the measured Rashba SOC strength exhibits a linear dependence on the applied gate voltage (*i.e.*, carrier density), and the magnitude of α_R can be tuned from 0.47 eV·Å (V_g = 0.9 V) to 0.73 eV·Å (V_g = −1.2 V), achieving a more than 50% modulation efficiency at T = 1.5 K.

Together with the temperature-dependent behaviors and quantitative band diagram simulation results using technology computer-aided design (TCAD), we propose that the band bending and Fermi level position (*i.e.*, carrier density) may exclusively determine the average Rashba coefficient of the n-type InSb(15 nm)/CdTe(1.2 μm) sample. Considering the top-gate configuration, the applied V_g is able to effectively modulate the overall carrier density of the InSb layer by a factor of 5, as illustrated in Figure 4c. According to the gate-dependent simulated band diagrams (inset of Figure 4c) and carrier density distribution profiles within the InSb layer (Figure 4e and Figure S8), it is seen that when V_g > 0 V is applied, a majority of the electrons with a high carrier density level would flow through the Al_2O_3/InSb interfacial channel, resulting in the bulk-dominated conduction featured by the negative MC background and weak WAL signature. On the other hand, the applied negative bias would drive the Fermi level position toward the InSb band gap center and change the band diagram to the opposite situation: The upward band bending brings about the electron depletion near the top Al_2O_3/InSb region, while an enhanced built-in electric field is generated at the bottom InSb/CdTe interface. Under such circumstances, both the larger WAL width (*i.e.*, higher $\boldsymbol{B}_{so}$) and the greatly reduced InSb layer carrier density (*i.e.*, smaller

https://dx.doi.org/10.1021/acsnano.0c07598
ACS Nano 2020, 14, 17396−17404

electron effective mass, see Figure S9) are expected to amplify the value of α_R in the $V_g > 0$ V region.

Finally, we choose the average Rashba coefficient (α_R) and its electric-field tunability ($d\alpha_R/d\mathbf{E}$) as the two figure-of-merits to benchmark material performance. As summarized in Table 1, our InSb/CdTe heterostructures hold both records (α_R = 0.7 eV·Å and $d\alpha_R/d\mathbf{E}$ = 60 eV·Å^2·V^{-1}) among all semiconductor-based candidates (*e.g.*, narrow-band III−V thin films/quantum wells/nanowires, oxide 2DEG, and large SOC 2D materials),[28,31,34−37,46,47] and our experiment data are comparable with the values estimated in topological hybrid systems.[21,22,48] Additionally, given the temperature-insensitive property of the Rashba SOC strength (Figure 3a), it is reasonable to speculate that the large α_R would persist to the high-temperature regime even though the absence of the WAL effect prevents us from quantifying the accurate value above 100 K. Finally, we need to mention that the magneto-transport characterization and the device configuration adopted in this work can only estimate the average Rashba SOC strength of the whole InSb/CdTe quantum well structures, since the electron effective mass is extracted from the overall carrier density through the ordinary Hall effect. In order to further distinguish the α_R contributions from the InSb/CdTe and Al_2O_3/InSb interfaces, an additional double-gated device and relevant multichannel transport model are needed in the follow-up study.

Table 1. Comparisons of the Average Rashba Coefficient α_R and Its Electric-Field Tunability $d\alpha_R/dE$ in Various Strong SOC Material Systems

strong SOC material systems	α_R (eV·Å)	$d\alpha_R/dE$ (eV·Å^2·V^{-1})
InSb/CdTe	0.4−0.7	60
InSb/InAlSb[31]	0.05−0.14	−
InAs/GaSb[35,47]	0.05−0.14	6.0
InAs nanowire[36]	0.06−0.2	14.4
$LaAlO_3/SrTiO_3$[28,46]	0.03−0.05	0.96
MoS_2[34]	0.04	1.1
Te[37]	0.054	0.3

CONCLUSION

In conclusion, we have shown the universal WAL phase diagram with a large Rashba coefficient, long phase-coherent length, and high onset temperature in the lattice-matched InSb/CdTe heterostructures. The enhancement of SOC may benefit from the improved InSb/CdTe interface quality with strong band bending. We have also demonstrated that the Rashba SOC strength at the InSb/CdTe interface can be optimized through both deliberate structural engineering and electric-field manipulation. By further adding another magnetic layer, we may explore the feasibility of energy-efficient spin−orbit torque-driven magnetization switching and spin-to-charge inversion in the hybrid system.[46,49,50] Governed by the same operational principle, the generic approach used in this work can also be transferred to other lattice-matched narrow-band III−V/II−VI heterostructures (*e.g.*, InAs/CdSe and InAsSb/ZnCdTe), and such a material integration concept may help construct a wide range of gate-controlled, ultralow-power spin−orbitronics applications.

EXPERIMENTAL METHODS

Sample Growth. The InSb/CdTe heterostructures growth was carried out in an ultrahigh-vacuum DCA dual-chamber MBE system. Semi-insulating ($\rho > 10^6$ Ω·cm) 3 in. GaAs (111) B wafers were preannealed in the growth chamber at up to 570 °C in order to remove the native oxide. To obtain a smooth surface morphology, a two-step growth procedure was adopted for the CdTe growth with a relatively low growth rate of 1.1 Å·s^{-1}. After a moderate postannealing at 355 °C, the CdTe film was exchanged onto another substrate holder and later transferred to the III−V chamber. For the subsequent InSb layer growth, the substrate temperature was kept at 300 °C, and the growth rate was fixed as 3.5 Å·s^{-1}. During the entire epitaxial growth, the beam flux monitor was used to calibrate element flux rate, and *in situ* RHEED was applied to monitor the real-time growth conditions.

Device Fabrication. The 3 in. InSb/CdTe wafers were patterned into μm-size six-probe Hall bar devices using conventional photolithography and ion-beam etching methods. Ti/Au (10 nm/190 nm) was deposited by *e*-beam evaporation to form the ohmic contacts after etching. A 50 nm-thick high-κ Al_2O_3 dielectric layer was deposited by atomic layer deposition (ALD) at 150 °C, and another Ti/Au (10 nm/90 nm) layer was deposited as the top-gate metal so as to complete the top-gated FET structure.

Transport Measurement. The magneto-transport measurements on both the mm-size Hall bar and μm-size top-gate FET devices were performed with a He-4 refrigerator (Oxford TeslatronPT system). Several experimental variables such as temperature, magnetic field, and lock-in frequency were varied during the measurements. Multiple lock-in amplifiers and Keithley source meters were connected to the samples to enable the precise four-point transport experiments for all devices.

Device Simulation. The Sentaurus TCAD device simulator from Synopsys was used to investigate the band diagram and carrier density profile of the top-gated InSb/CdTe device. A typical Al_2O_3(50 nm)/InSb(15 nm)/CdTe(1.2 μm) MOS structure was defined by the SDE tools. The dielectric constant of Al_2O_3 was set to 8.6 in reference to the capacitance test result of our ALD grown Al_2O_3 thin film. During the simulation process, the gate electrode was placed at the top of the Al_2O_3 layer, and ground electrodes were placed at the right/left edge of the InSb channel. The designed device structure was later exported to the SDevice tool in which the 2D Poisson solver including both electron and hole was performed to obtain the real-space band diagram and carrier distribution under different gate voltage bias.

ASSOCIATED CONTENT

Supporting Information

The Supporting Information is available free of charge at https://pubs.acs.org/doi/10.1021/acsnano.0c07598.

> Magento-resistance data of the InSb/CdTe heterostructures, data fitting and parameter extraction from the WAL results, temperature-dependent phase-coherent length of the InSb/CdTe samples, correlation between the spin−orbit relaxation time and the momentum-scattering time, temperature-dependent longitudinal conductance in the InSb/CdTe heterostructures, temperature-dependent Rashba SOC in the InSb/CdTe heterostructures, temperature-dependent magnetoconductance plots of samples A and B, carrier-density distribution of the Al_2O_3/InSb(15 nm)/CdTe device under different gate bias, gate voltage-dependent electron effective mass in the InSb/CdTe heterostructures (PDF)

https://dx.doi.org/10.1021/acsnano.0c07598
ACS Nano 2020, 14, 17396−17404

AUTHOR INFORMATION

Corresponding Author

Xufeng Kou − *School of Information Science and Technology and ShanghaiTech Laboratory for Topological Physics, ShanghaiTech University, Shanghai 200031, China;* orcid.org/0000-0002-8860-5105; Email: kxf2323@gmail.com

Authors

Yong Zhang − *School of Information Science and Technology, ShanghaiTech University, Shanghai 200031, China; Shanghai Institute of Microsystem and Information Technology, Chinese Academy of Sciences, Shanghai 200050, China; University of Chinese Academy of Sciences, Beijing 101408, China;* orcid.org/0000-0002-3442-6646

Fenghua Xue − *School of Information Science and Technology, ShanghaiTech University, Shanghai 200031, China; Shanghai Institute of Microsystem and Information Technology, Chinese Academy of Sciences, Shanghai 200050, China; University of Chinese Academy of Sciences, Beijing 101408, China*

Chenjia Tang − *ShanghaiTech Laboratory for Topological Physics and School of Physical Science and Technology, ShanghaiTech University, Shanghai 200031, China*

Jiaming Li − *School of Information Science and Technology, ShanghaiTech University, Shanghai 200031, China; Shanghai Institute of Microsystem and Information Technology, Chinese Academy of Sciences, Shanghai 200050, China; University of Chinese Academy of Sciences, Beijing 101408, China*

Liyang Liao − *Key Lab Advanced Materials (MOE), School of Materials Science and Engineering, Tsinghua University, Beijing 100084, China*

Lun Li − *School of Information Science and Technology, ShanghaiTech University, Shanghai 200031, China; Shanghai Institute of Microsystem and Information Technology, Chinese Academy of Sciences, Shanghai 200050, China; University of Chinese Academy of Sciences, Beijing 101408, China*

Xiaoyang Liu − *School of Information Science and Technology, ShanghaiTech University, Shanghai 200031, China; Shanghai Institute of Microsystem and Information Technology, Chinese Academy of Sciences, Shanghai 200050, China; University of Chinese Academy of Sciences, Beijing 101408, China*

Yumeng Yang − *School of Information Science and Technology, ShanghaiTech University, Shanghai 200031, China*

Cheng Song − *Key Lab Advanced Materials (MOE), School of Materials Science and Engineering, Tsinghua University, Beijing 100084, China;* orcid.org/0000-0002-7651-9031

Complete contact information is available at:
https://pubs.acs.org/10.1021/acsnano.0c07598

Author Contributions

[∇]These authors contributed equally to this work.

Notes

The authors declare no competing financial interest.

ACKNOWLEDGMENTS

We are grateful to the insightful discussions from Dr. Shun-Qing Shen, Dr. Bo Fu, and Dr. Huan-wen Huang from University of Hong Kong. This work is supported by the National Key R&D Program of China (contract no. 2017YFB0405704), the National Natural Science Foundation of China (grant no. 61874172), the Strategic Priority Research Program of Chinese Academy of Sciences (grant no. XDA18010000), the Major Project of Shanghai Municipal Science and Technology (grant no. 2018SHZDZX02), and the Shanghaitech Quantum Device and Soft Matter Nano-fabrication Laboratories (SMN180827). X.K. acknowledges the support from the Merck POC program.

REFERENCES

(1) Sinova, J.; Valenzuela, S. O.; Wunderlich, J.; Back, C. H.; Jungwirth, T. Spin Hall Effects. *Rev. Mod. Phys.* **2015**, *87* (4), 1213−1259.

(2) Koo, H. C.; Kwon, J. H.; Eom, J.; Chang, J.; Han, S. H.; Johnson, M. Control of Spin Precession in a Spin-Injected Field Effect Transistor. *Science* **2009**, *325* (5947), 1515−1518.

(3) Miron, I. M.; Gaudin, G.; Auffret, S.; Rodmacq, B.; Schuhl, A.; Pizzini, S.; Vogel, J.; Gambardella, P. Current-Driven Spin Torque Induced by the Rashba Effect in a Ferromagnetic Metal Layer. *Nat. Mater.* **2010**, *9* (3), 230−234.

(4) Liu, L. Q.; Pai, C. F.; Li, Y.; Tseng, H. W.; Ralph, D. C.; Buhrman, R. A. Spin-Torque Switching with the Giant Spin Hall Effect of Tantalum. *Science* **2012**, *336* (6081), 555−558.

(5) Rojas Sanchez, J. C.; Vila, L.; Desfonds, G.; Gambarelli, S.; Attane, J. P.; De Teresa, J. M.; Magen, C.; Fert, A. Spin-to-Charge Conversion Using Rashba Coupling at the Interface between Non-Magnetic Materials. *Nat. Commun.* **2013**, *4*, 2944.

(6) Chuang, P.; Ho, S. C.; Smith, L. W.; Sfigakis, F.; Pepper, M.; Chen, C. H.; Fan, J. C.; Griffiths, J. P.; Farrer, I.; Beere, H. E.; Jones, G. A. C.; Ritchie, D. A.; Chen, T. M. All-Electric All-Semiconductor Spin Field-Effect Transistors. *Nat. Nanotechnol.* **2015**, *10* (1), 35−39.

(7) Kane, C. L.; Mele, E. J. Z_2 Topological Order and the Quantum Spin Hall Effect. *Phys. Rev. Lett.* **2005**, *95* (14), 146802.

(8) Bernevig, B. A.; Hughes, T. L.; Zhang, S. C. Quantum Spin Hall Effect and Topological Phase Transition in HgTe Quantum Wells. *Science* **2006**, *314* (5806), 1757−1761.

(9) Pesin, D.; MacDonald, A. H. Spintronics and Pseudospintronics in Graphene and Topological Insulators. *Nat. Mater.* **2012**, *11* (5), 409−416.

(10) Young, S. M.; Zaheer, S.; Teo, J. C. Y.; Kane, C. L.; Mele, E. J.; Rappe, A. M. Dirac Semimetal in Three Dimensions. *Phys. Rev. Lett.* **2012**, *108* (14), 140405.

(11) Mellnik, A. R.; Lee, J. S.; Richardella, A.; Grab, J. L.; Mintun, P. J.; Fischer, M. H.; Vaezi, A.; Manchon, A.; Kim, E. A.; Samarth, N.; Ralph, D. C. Spin-Transfer Torque Generated by a Topological Insulator. *Nature* **2014**, *511* (7510), 449−451.

(12) Fan, Y. B.; Upadhyaya, P.; Kou, X. F.; Lang, M. R.; Takei, S.; Wang, Z. X.; Tang, J. S.; He, L.; Chang, L. T.; Montazeri, M.; Yu, G. Q.; Jiang, W. J.; Nie, T. X.; Schwartz, R. N.; Tserkovnyak, Y.; Wang, K. L. Magnetization Switching through Giant Spin-Orbit Torque in a Magnetically Doped Topological Insulator Heterostructure. *Nat. Mater.* **2014**, *13* (7), 699−704.

(13) Weng, H. M.; Fang, C.; Fang, Z.; Bernevig, B. A.; Dai, X. Weyl Semimetal Phase in Noncentrosymmetric Transition-Metal Monophosphides. *Phys. Rev. X* **2015**, *5* (1), No. 011029.

(14) Nitta, J.; Akazaki, T.; Takayanagi, H.; Enoki, T. Gate Control of Spin-Orbit Interaction in an Inverted $In_{0.53}Ga_{0.47}As/In_{0.52}Al_{0.48}As$ Heterostructure. *Phys. Rev. Lett.* **1997**, *78* (7), 1335−1338.

(15) Winkler, R.; Papadakis, S.; De Poortere, E.; Shayegan, M., Inversion-Asymmetry-Induced Spin Splitting. *Spin-Orbit Coupling in Two-Dimensional Electron and Hole Systems*, 3rd ed.; Springer: Berlin, Germany, 2003; Vol. *41*, pp 69−130.

(16) Ganichev, S. D.; Bel'kov, V. V.; Golub, L. E.; Ivchenko, E. L.; Schneider, P.; Giglberger, S.; Eroms, J.; De Boeck, J.; Borghs, G.; Wegscheider, W.; Weiss, D.; Prettl, W. Experimental Separation of

Rashba and Dresselhaus Spin Splittings in Semiconductor Quantum Wells. *Phys. Rev. Lett.* **2004**, *92* (25), 256601.
(17) Manchon, A.; Koo, H. C.; Nitta, J.; Frolov, S. M.; Duine, R. A. New Perspectives for Rashba Spin-Orbit Coupling. *Nat. Mater.* **2015**, *14* (9), 871−882.
(18) Soumyanarayanan, A.; Reyren, N.; Fert, A.; Panagopoulos, C. Emergent Phenomena Induced by Spin-Orbit Coupling at Surfaces and Interfaces. *Nature* **2016**, *539* (7630), 509−517.
(19) Wang, K. L.; Kou, X. F.; Upadhyaya, P.; Fan, Y. B.; Shao, Q. M.; Yu, G. Q.; Amiri, P. K. Electric-Field Control of Spin-Orbit Interaction for Low-Power Spintronics. *Proc. IEEE* **2016**, *104* (10), 1974−2008.
(20) Yaji, K.; Ohtsubo, Y.; Hatta, S.; Okuyama, H.; Miyamoto, K.; Okuda, T.; Kimura, A.; Namatame, H.; Taniguchi, M.; Aruga, T. Large Rashba Spin Splitting of a Metallic Surface-State Band on a Semiconductor Surface. *Nat. Commun.* **2010**, *1*, 17.
(21) Rojas-Sanchez, J. C.; Oyarzun, S.; Fu, Y.; Marty, A.; Vergnaud, C.; Gambarelli, S.; Vila, L.; Jamet, M.; Ohtsubo, Y.; Taleb-Ibrahimi, A.; Le Fevre, P.; Bertran, F.; Reyren, N.; George, J. M.; Fert, A. Spin to Charge Conversion at Room Temperature by Spin Pumping into a New Type of Topological Insulator: A-Sn Films. *Phys. Rev. Lett.* **2016**, *116* (9), No. 096602.
(22) Shi, S. Y.; Wang, A. Z.; Wang, Y.; Ramaswamy, R.; Shen, L.; Moon, J.; Zhu, D. P.; Yu, J. W.; Oh, S.; Feng, Y. P.; Yang, H. Efficient Charge-Spin Conversion and Magnetization Switching through the Rashba Effect at Topological-Insulator/Ag Interfaces. *Phys. Rev. B: Condens. Matter Mater. Phys.* **2018**, *97* (4), No. 041115.
(23) Gilbertson, A. M.; Branford, W. R.; Fearn, M.; Buckle, L.; Buckle, P. D.; Ashley, T.; Cohen, L. F. Zero-Field Spin Splitting and Spin-Dependent Broadening in High-Mobility $InSb/In_{1-X}Al_xSb$ Asymmetric Quantum Well Heterostructures. *Phys. Rev. B: Condens. Matter Mater. Phys.* **2009**, *79* (23), 235333.
(24) Mackey, K. J.; Allen, P. M. G.; Herrendenharker, W. G.; Williams, R. H.; Whitehouse, C. R.; Williams, G. M. Chemical and Electronic-Structure of InSb-CdTe Interfaces. *Appl. Phys. Lett.* **1986**, *49* (6), 354−356.
(25) Sze, S. M.; Ng, K. K., Metal-Insulator-Semiconductor Capacitors. *Physics of Semiconductor Devices*, 3rd ed.; John Wiley & Sons: Hoboken, NJ, 2006; pp 197−240.
(26) Liu, Q. H.; Zhang, X. W.; Abdalla, L. B.; Zunger, A. Transforming Common III-V and II-VI Semiconductor Compounds into Topological Heterostructures: The Case of CdTe/InSb Superlattices. *Adv. Funct. Mater.* **2016**, *26* (19), 3259−3267.
(27) Li, J.; Tang, C.; Du, P.; Jiang, Y.; Zhang, Y.; Zhao, X.; Gong, Q.; Kou, X. Epitaxial Growth of Lattice-Matched InSb/CdTe Heterostructures on the GaAs(111) Substrate by Molecular Beam Epitaxy. *Appl. Phys. Lett.* **2020**, *116* (12), 122102.
(28) Caviglia, A. D.; Gabay, M.; Gariglio, S.; Reyren, N.; Cancellieri, C.; Triscone, J. M. Tunable Rashba Spin-Orbit Interaction at Oxide Interfaces. *Phys. Rev. Lett.* **2010**, *104* (12), 126803.
(29) Bercioux, D.; Lucignano, P. Quantum Transport in Rashba Spin-Orbit Materials: A Review. *Rep. Prog. Phys.* **2015**, *78* (10), 106001.
(30) Koga, T.; Nitta, J.; Akazaki, T.; Takayanagi, H. Rashba Spin-Orbit Coupling Probed by the Weak Antilocalization Analysis in InAlAs/InGaAs/InAlAs Quantum Wells as a Function of Quantum Well Asymmetry. *Phys. Rev. Lett.* **2002**, *89* (4), No. 046801.
(31) Kallaher, R. L.; Heremans, J. J.; Goel, N.; Chung, S. J.; Santos, M. B. Spin-Orbit Interaction Determined by Antilocalization in an InSb Quantum Well. *Phys. Rev. B: Condens. Matter Mater. Phys.* **2010**, *81* (7), No. 075303.
(32) Nakamura, H.; Koga, T.; Kimura, T. Experimental Evidence of Cubic Rashba Effect in an Inversion-Symmetric Oxide. *Phys. Rev. Lett.* **2012**, *108* (20), 206601.
(33) Lang, M. R.; He, L.; Kou, X. F.; Upadhyaya, P.; Fan, Y. B.; Chu, H.; Jiang, Y.; Bardarson, J. H.; Jiang, W. J.; Choi, E. S.; Wang, Y.; Yeh, N. C.; Moore, J.; Wang, K. L. Competing Weak Localization and Weak Antilocalization in Ultrathin Topological Insulators. *Nano Lett.* **2013**, *13* (1), 48−53.
(34) Schmidt, H.; Yudhistira, I.; Chu, L.; Neto, A. H. C.; Ozyilmaz, B.; Adam, S.; Eda, G. Quantum Transport and Observation of Dyakonov-Perel Spin-Orbit Scattering in Monolayer MoS_2. *Phys. Rev. Lett.* **2016**, *116* (4), No. 046803.
(35) Herling, F.; Morrison, C.; Knox, C. S.; Zhang, S.; Newell, O.; Myronov, M.; Linfield, E. H.; Marrows, C. H. Spin-Orbit Interaction in InAs/GaSb Heterostructures Quantified by Weak Antilocalization. *Phys. Rev. B: Condens. Matter Mater. Phys.* **2017**, *95* (15), 155307.
(36) Takase, K.; Ashikawa, Y.; Zhang, G.; Tateno, K.; Sasaki, S. Highly Gate-Tuneable Rashba Spin-Orbit Interaction in a Gate-All-Around InAs Nanowire Metal-Oxide-Semiconductor Field-Effect Transistor. *Sci. Rep.* **2017**, *7*, 930.
(37) Niu, C.; Qiu, G.; Wang, Y. X.; Zhang, Z. X.; Si, M. W.; Wu, W. Z.; Ye, P. D. D. Gate-Tunable Strong Spin-Orbit Interaction in Two-Dimensional Tellurium Probed by Weak Antilocalization. *Phys. Rev. B: Condens. Matter Mater. Phys.* **2020**, *101* (20), 205414.
(38) Knap, W.; Skierbiszewski, C.; Zduniak, A.; LitwinStaszewska, E.; Bertho, D.; Kobbi, F.; Robert, J. L.; Pikus, G. E.; Pikus, F. G.; Iordanskii, S. V.; Mosser, V.; Zekentes, K.; LyandaGeller, Y. B. Weak Antilocalization and Spin Precession in Quantum Wells. *Phys. Rev. B: Condens. Matter Mater. Phys.* **1996**, *53* (7), 3912−3924.
(39) Leontiadou, M. A.; Litvinenko, K. L.; Gilbertson, A. M.; Pidgeon, C. R.; Branford, W. R.; Cohen, L. F.; Fearn, M.; Ashley, T.; Emeny, M. T.; Murdin, B. N.; Clowes, S. K. Experimental Determination of the Rashba Coefficient in Insb/Inalsb Quantum Wells at Zero Magnetic Field and Elevated Temperatures. *J. Phys.: Condens. Matter* **2011**, *23* (3), No. 035801.
(40) Altshuler, B. L.; Aronov, A. G.; Khmelnitsky, D. E. Effects of Electron-Electron Collisions with Small Energy Transfers on Quantum Localization. *J. Phys. C: Solid State Phys.* **1982**, *15* (36), 7367.
(41) Dyakonov, M. I.; Perel, V. I. Current-Induced Spin Orientation of Electrons in Semiconductors. *Phys. Lett. A* **1971**, *35* (6), 459−460.
(42) Lu, H. Z.; Shen, S. Q. Finite-Temperature Conductivity and Magnetoconductivity of Topological Insulators. *Phys. Rev. Lett.* **2014**, *112* (14), 146601.
(43) Sniadower, L.; Rauluszkiewicz, J.; Galazka, R. R. Determination of the Effective Mass in n-Type InSb by Means of Magneto-Plasma Reflection. *Phys. Status Solidi B* **1964**, *6* (2), 549−554.
(44) Liu, R. H.; Lim, W. L.; Urazhdin, S. Control of Current-Induced Spin-Orbit Effects in a Ferromagnetic Heterostructure by Electric Field. *Phys. Rev. B: Condens. Matter Mater. Phys.* **2014**, *89* (22), 220409.
(45) Fan, Y. B.; Kou, X. F.; Upadhyaya, P.; Shao, Q. M.; Pan, L.; Lang, M. R.; Che, X. Y.; Tang, J. S.; Montazeri, M.; Murata, K.; Chang, L. T.; Akyol, M.; Yu, G. Q.; Nie, T. X.; Wong, K. L.; Liu, J.; Wang, Y.; Tserkovnyak, Y.; Wang, K. L. Electric-Field Control of Spin-Orbit Torque in a Magnetically Doped Topological Insulator. *Nat. Nanotechnol.* **2016**, *11* (4), 352−359.
(46) Lesne, E.; Fu, Y.; Oyarzun, S.; Rojas-Sanchez, J. C.; Vaz, D. C.; Naganuma, H.; Sicoli, G.; Attane, J. P.; Jamet, M.; Jacquet, E.; George, J. M.; Barthelemy, A.; Jaffres, H.; Fert, A.; Bibes, M.; Vila, L. Highly Efficient and Tunable Spin-to-Charge Conversion through Rashba Coupling at Oxide Interfaces. *Nat. Mater.* **2016**, *15* (12), 1261−1266.
(47) Beukman, A. J. A.; de Vries, F. K.; van Veen, J.; Skolasinski, R.; Wimmer, M.; Qu, F. M.; de Vries, D. T.; Nguyen, B. M.; Yi, W.; Kiselev, A. A.; Sokolich, M.; Manfra, M. J.; Nichele, F.; Marcus, C. M.; Kouwenhoven, L. P. Spin-Orbit Interaction in a Dual Gated InAs/GaSb Quantum Well. *Phys. Rev. B: Condens. Matter Mater. Phys.* **2017**, *96* (24), 241401.
(48) Zhu, Z. H.; Levy, G.; Ludbrook, B.; Veenstra, C. N.; Rosen, J. A.; Comin, R.; Wong, D.; Dosanjh, P.; Ubaldini, A.; Syers, P.; Butch, N. P.; Paglione, J.; Elfimov, I. S.; Damascelli, A. Rashba Spin-Splitting Control at the Surface of the Topological Insulator Bi_2Se_3. *Phys. Rev. Lett.* **2011**, *107* (18), 186405.
(49) Ganichev, S. D.; Ivchenko, E. L.; Danilov, S. N.; Eroms, J.; Wegscheider, W.; Weiss, D.; Prettl, W. Conversion of Spin into Directed Electric Current in Quantum Wells. *Phys. Rev. Lett.* **2001**, *86* (19), 4358−4361.

https://dx.doi.org/10.1021/acsnano.0c07598
ACS Nano 2020, 14, 17396−17404

(50) Shao, Q.; Wu, H.; Pan, Q.; Zhang, P.; Pan, L.; Wong, K.; Che, X.; Wang, K. L. Room Temperature Highly Efficient Topological Insulator/Mo/Cofeb Spin-Orbit Torque Memory with Perpendicular Magnetic Anisotropy. Proceedings from the *IEEE International Electron Devices Meeting (IEDM)*, San Francisco, CA, December 1–5, 2018; IEEE: New York, 2018; pp 36.3. 1–36.3. 4.

https://dx.doi.org/10.1021/acsnano.0c07598
ACS Nano 2020, 14, 17396–17404